Chemical Engineering Journal 499 (2024) 156050

Contents lists available at ScienceDirect

Chemical Engineering Journal

journal homepage: www.elsevier.com/locate/cej

Biomimetic Fe^{3+} metal-phenolic networks enable DNAzyme and Cas9 RNP delivery for synergistic tumor ferroptosis-immunotherapy

Chao Chen [a,*,1], Xueting Shen [a,1], Silin Shi [a], Yin Xu [a], Hongxiu Song [a], Lihua Qu [b], Shiyu Du [c], Yamei Gao [d], Xin Han [a,*]

[a] The Second Affiliated Hospital of Nanjing University of Chinese Medicine, Jiangsu Collaborative Innovation Center of Chinese Medicinal Resources Industrialization, School of Medicine, Nanjing University of Chinese Medicine, Nanjing 210023, China
[b] School of Basic Medical Sciences, Xianning Medical College, Hubei University of Science and Technology, Hubei 437000, China
[c] College of Engineering and Applied Sciences, Nanjing University, Nanjing 210023, China
[d] Department of Dermatology, First Affiliated Hospital of Nanjing Medical University and Jiangsu Province People's Hospital, Nanjing 210029, China

ARTICLE INFO

Keywords:
Metal-phenolic networks
DNAzyme
Cas9 RNP
Ferroptosis
Tumor immunotherapy

ABSTRACT

Ferroptosis has the potential to induce powerful antitumor immunity by activating immunogenic cell death (ICD) of tumor cells. However, achieving precise and effective ferroptosis-immunotherapy remains challenging. Herein, a biomimetic metal-phenolic networks (MPNs) nanosystem was proposed for codelivery of Cas9 ribonucleoprotein (RNP) and DNAzyme systems to achieve robust synergistic ferroptosis-immunotherapy. The nanosystem was consisted of MPNs containing tannic acid (TA) and Fe^{3+} ions, the Cas9 RNP and DNAzyme systems, which were released and exerted their respective functions after intracellular delivery with the aid of erythrocyte membrane camouflage. The Fe^{2+} ions were produced from Fe^{3+} by TA reduction to assist in endosomal escape and induced ferroptosis. Cas9 RNP entered into the nucleus and executed gene editing of GPX4 to enhance ferroptosis and thus induce ICD. Simultaneously, Fe^{2+} assisted DNAzyme system was activated to silence GPR65 gene expression to further achieve synergistic ferroptosis-immune responses, resulting in the eradication of both orthotopic and pulmonary metastatic tumors. Overall, this biomimetic nanosystem provides a versatile strategy for synergistic gene editing, ferroptosis, and immunotherapy to achieve robust ferroptosis-immunotherapy.

1. Introduction

As an iron-regulated unique form of programmed cell death, ferroptosis is quite different from apoptosis, necrosis and autophagy, and is mediated by iron-dependent accumulation of lipid peroxidation (LPO) [1,2]. Ferroptosis has recently attracted considerable attention as a potential cancer therapeutic method [3,4]. The limited function of glutathione peroxidase 4 (GPX4) or excessive LPO can directly or indirectly induce ferroptosis, and leading to a large accumulation of lipid peroxides and eventually triggers cell death [5,6]. Notably, GPX4 is the only glutathione peroxidase in the cell responsible for reducing lipid peroxides by converting peroxy bonds into hydroxyl groups through a specific biochemical process that deactivates lipid peroxides [7–9]. Studies have shown that GPX4 and ferroptosis involve in the pathophysiology of several diseases, including cancer [10]. Moreover, as the cystine/glutamate antiporter system, System Xc^- contains two essential subunits (SLC7A11 and SLC3A2) that directly inhibit ferroptosis by regulating the intracellular glutathione levels and GPX4 activity. Conversely, interferon-γ (IFN-γ) is a crucial cytokine produced by activated immune cells, and it has been reported that IFN-γ can indirectly alter the susceptibility of tumor cells to ferroptosis by interacting with the immune system and possibly iron homeostasis [11].

Metal-phenolic networks (MPNs), as a new organic–inorganic hybrid network system, have received extensive attention in recent years [12–14]. Among them, Fe-based MPNs shows the excellent stability, controllability, versatility and high drug loading capacity and has the potential as a ferroptosis nano inducers [15]. As a naturally occurring polyphenol extracted from plant, tannic acid (TA) can serve as chelating sites for multivalent metal ions due to its rich digalloyl groups and form stable organometallic MPNs [16]. However, the challenges of synthesis

* Corresponding authors.
E-mail addresses: cchen22@njucm.edu.cn (C. Chen), xhan0220@njucm.edu.cn (X. Han).
[1] These authors contributed equally.

https://doi.org/10.1016/j.cej.2024.156050
Received 14 June 2024; Received in revised form 18 September 2024; Accepted 20 September 2024
Available online 22 September 2024

difficulties, potential toxicity, and poor biocompatibility still need to be addressed for practical applications [17]. Compared with the conventional nanosystems, the erythrocyte membrane (EM) camouflaged nanoparticle has the preferable characteristics of prolonged circulation time in vivo, enhanced phagocytosis resistance, and immune evasion by mimicking the function of erythrocyte, which enables higher biocompatibility and stability [18,19]. Therefore, EM based biomimetic delivery have shown broad application prospects in many fields such as drug delivery, tumor therapy, and biological imaging [20,21].

Recently, the strategy of combining ferroptosis mechanism with immunotherapy has shown excellent efficacy in cancer treatment [15,22]. Studies have shown that the combined application of immunotherapy and ferroptosis can produce amplified anti-tumor efficiency [23,24]. With the further development of ferroptosis, damage-associated molecular patterns (DAMP) are released, suggesting the occurrence of immunogenic cell death (ICD) in tumor cells [25–27]. The ICD process activates cytotoxic T lymphocytes (CTLs) through the antigen-presenting mechanism, which further triggers a new round of ferroptosis-immunotherapy cascade and exponentially amplifies the therapeutic effects [28–30]. As an innate immune checkpoint gene, G-protein-coupled receptor (GPR65) has a profound impact on the tumor microenvironment by inhibiting the release of inflammatory factors and inducing up-regulation of tissue repair genes [31,32]. Studies have indicated that downregulation of GPR65 can decrease the expression of PD-L1 in melanoma [33]. CRISPR-Cas9 gene editing system is the most widely used type II CRISPR system and has great potential for tumor gene therapy [34,35]. DNAzyme has been widely used in gene therapy because of its remarkable metal ion catalyzed RNA splitting property [36–38]. The ingenious combination of DNAzyme and CRISPR-Cas9 system can precisely regulate the expression of dual target genes from both of the transcription and translation levels, showing unprecedented accuracy and efficiency.

In this study, we proposed an EM-based biomimetic MPNs nanosystem for co-delivery of Cas9 ribonucleoprotein (RNP) and DNAzyme systems to achieve robust synergistic ferroptosis-immunotherapy. During the process of nanosystem synthesis, TA combines with Fe^{3+} to form the TA-Fe (TF) MPNs and subsequently modified with cationic polyelectrolyte (poly(allylamine hydrochloride), PAH) (TF@P). Cas9 RNP and DNAzyme systems were electrostatically adsorbed on TF, and then encapsulated with EM to form the final DR-TF@E nanosystem (Fig. 1A). After intracellular delivery with the assistance of EM camouflage, the MPNs degraded into TA and Fe^{3+}, in which Fe^{2+} ions were produced from Fe^{3+} by TA reduction to assist in endosomal escape and induced ferroptosis. Meanwhile, gene editing of GPX4 by the Cas9 RNP enhanced ferroptosis and induced ICD, which synergized with Fe^{2+} assisted DNAzyme system for gene silencing of GPR65, to realize synergistic ferroptosis-immunotherapy (Fig. 1B). By synergistic combination with ferroptosis, immunotherapy, and gene therapy, this biomimetic nanosystem provides a versatile tumor therapeutic strategy with highly efficiency and safety.

2. Results and Discussion

2.1. Synthesis and characterization of DR-TF@E nanosystem

Nanosized networks, TF was firstly assembled using tannic acid (TA) coordinated with metal complex of Fe^{3+} and characterized by the transmission electron microscope (TEM) and dynamic light scattering

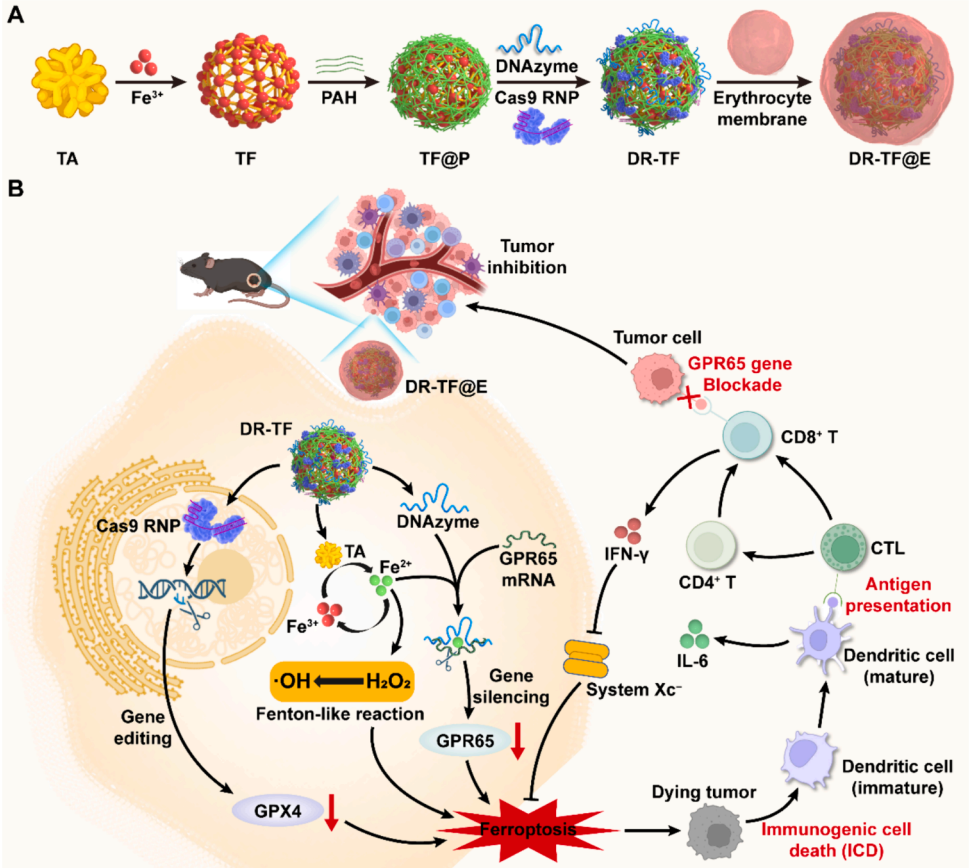

Fig. 1. Design of biomimetic Fe^{3+} metal-phenolic networks for gene regulation of GPX4 and GPR65 to realize synergistic tumor ferroptosis-immunotherapy. A) The synthesis process of DR-TF@E nanosystem. B) DR-TF@E achieved synergistic tumor ferroptosis-immunotherapy by Cas9 RNP mediated GPX4 gene editing and DNAzyme mediated GPR65 gene silencing.

(DLS). It was shown that TF appeared good dispersity under TEM observation (Fig. S1A) and had a hydrodynamic diameter of 125.6 ± 2.7 nm (Fig. S1B). Then, the sgRNA was synthesized and verified by gel electrophoresis (Figure S2) and the TF was directly mixed with the cationic PAH and the Cas9 RNP and DNAzyme systems was encapsulated subsequently to synthesis the DR-TF@P. DR-TF@E nanosystem was obtained by the outermost layer modification of the erythrocyte membrane (EM), which improved the stability and targeting property of the nanosystem (Fig. 2A). The synthetic process of DR-TF@E was monitored using the TEM imaging, DLS and ζ potential measurements. DR-TF@E appeared in spherical shape with good dispersibility under the TEM imaging (Fig. 2B) and had an increased hydrodynamic diameter of 226.6 ± 34.2 nm (Fig. 2C). The results indicated an obvious decreased of ζ potential from + 50.7 ± 1.53 mV (TF@P) to + 31.2 ± 1.2 mV (DR-TF@P) after encapsulated with the Cas9 RNP and DNAzyme system, and then down to a negative value (DR-TF@E, −4.3 ± 0.1 mV) after modified with the EM (Fig. 2D). The changes in hydrodynamic diameter and ζ potential suggested the successful synthesis of the DR-TF@E nanosystem (Figure S3). The XPS spectrum of TF complex showed the peaks of Fe 2p (711 eV), O 1 s (532 eV), N 1 s (399 eV), and C 1 s (286 eV), indicating the successful coordination of Fe(III) (Fig. S4A). According to the standard binding energy lookup table, the two strong binding energy peaks at 711 and 724 eV, belonging to Fe(III) 2p3/2 and Fe(III) 2p1/2, respectively, which verified that the Fe in TF complex was ferric irons (Fig. S4B). Moreover, the harvested EM was confirmed using the TEM imaging (Figure S5), and the integrity of EM on DR-TF@E nanosystem was studied using gel electrophoresis analysis (Figure S6), which indicated that the composition of membrane proteins was largely preserved and similar to that of the EM controls. To verify the enhanced cellular endocytosis property of EM modified nanosystem, the FAM-labeled nanosystem was assembled and the results indicated that the DR-TF@E with EM coating could obviously enter into the tumor cells compared with the DR-TF without EM coating (Figure S7), thus enhanced the in vitro antitumor effects of nanosystem. The stability of DR-TF@E nanosystem with EM coating was also confirmed in a variety of solutions (H_2O, PBS, and DMEM), and found that the nanosystem could exist stably in a variety of solutions for a long time (at least 24 h) (Figure S8A–C), which suggesting the in vitro stability of nanosystem.

To further determine the loading capacity of TF@P encapsulating Cas9 RNP and DNAzyme systems, FAM-labeled DNAzyme complex was used and it was indicated that DR-TF@E showed a favorable loading capacity of DNAzyme system (Fig. 2E), that is, FAM-labeled DNAzyme gradually loaded with the increase of TF proportion. FITC-labeled Cas9 nuclease was also employed to detect the loading efficiency of the Cas9 RNP in DR-TF@E nanosystem, and the results demonstrated that Cas9 nuclease was gradually loaded with the increase of TF amount, suggesting that DR-TF@E had a good loading efficiency for Cas9 RNP (Figure S9). We also detected whether the ratio of Cas9 RNP to DNAzyme affected the loading capacity of TF@P and it was found that the change in ratio of Cas9 RNP to DNAzyme had little effect on the loading capacity of TF@P (Figure S10). Meanwhile, the cargo release ability of DR-TF@E nanosystem was measured under the mimic tumor microenvironment (TME) conditions and FITC-labeled Cas9 protein was employed to indicate the loading cargo. It was found that the fluorescence intensity was obviously gradually increased with the increasing incubation time (0, 2, 8, 12 h) and decreasing pH value (pH 7.4, 6.0, and 5.0) (Figure S11A-B), which indicated that DR-TF@E nanosystem could successfully release the loading cargo under the TME. After completing the structure verification of nanosystem, the functional properties were further explored. Fe^{3+} in nanosystem could gradually reduce to Fe^{2+} through TA under TME condition, and it was shown that the percentage of Fe^{2+} upregulated as the pH value decreased from 7.4 to 5.0, especially approximately 64 % of Fe^{3+} was reduced to Fe^{2+} within 1 h at pH 5.0 (Fig. 2F and Figure S12A). The methylene blue (MB) detection was

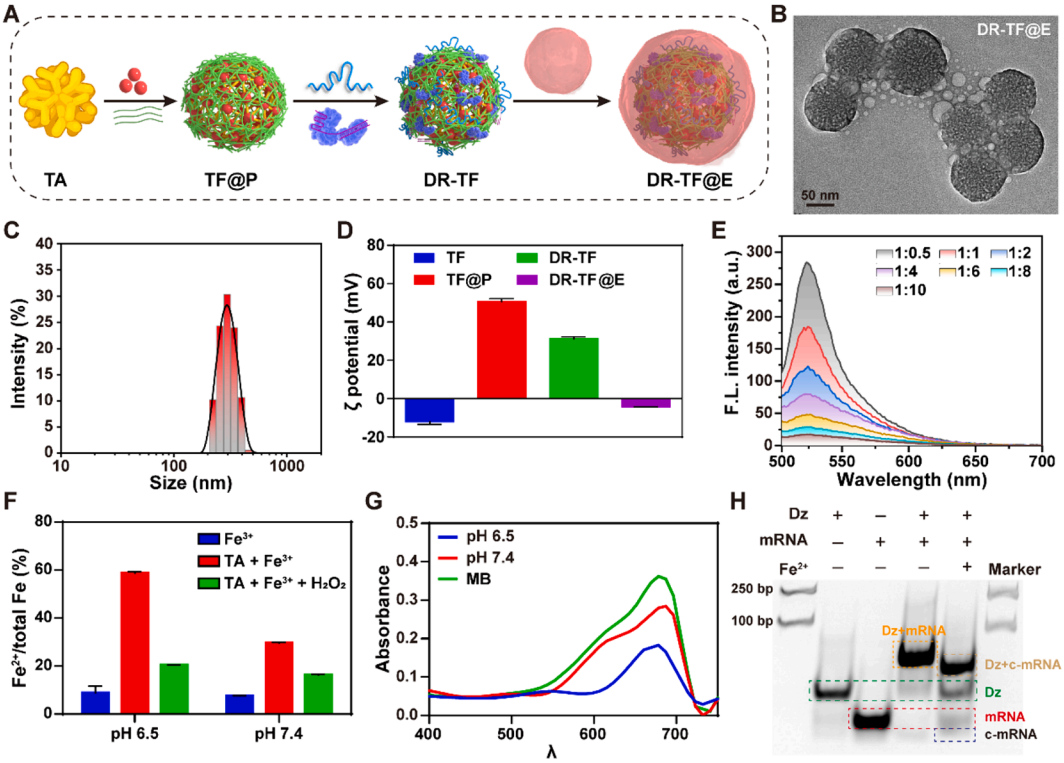

Fig. 2. Characterization of Biomimetic Fe^{3+} metal-phenolic networks. A) Synthesis process of DR-TF@E nanosystem. B) Representative TEM images of DR-TF@E nanosystem. Scale bar: 50 nm. C) Hydrodynamic diameters of DR-TF@E. D) ζ potentials of different intermediates during the synthesis of DR-TF@E nanosystem. E) Fluorescence intensity of free FAM-labeled DNAzyme after TF adsorption at different DNAzyme/TF@P ratios. F) Measurement of Fe^{2+} content under different pH conditions; G) Degradation rate of MB at pH 6.5 or 7.4 in the presence of H_2O_2. H) Native-gel electrophoresis image shows the cleavage activity of DNAzyme for mRNA substrate of GPR65. Dz: DNAzyme; c-mRNA: cleaved mRNA; Results are represented as means ± SD (n = 3).

employed to detect the Fenton reaction initiated by in situ generated the Fe^{2+} interacted with H_2O_2 (Fig. 2G and Figure S12B), and the Fe^{3+} was regenerated subsequently with reactive oxygen species (ROS) production and continually the next round of reaction. Notably, the Fe^{2+} converted from the DR-TF@E under TME could be used as the metal cofactor of DNAzyme system for RNA cleavage and the GPR65 mRNA substrate was employed. The result indicated that the designed DNAzyme system could effectively cleave the GPR65 mRNA substrate, of which the Dz + c-mRNA band in Dz + mRNA + Fe^{2+} channel was slightly lower than the Dz + mRNA band in Dz + mRNA channel as well as the appearance of c-mRNA band, suggesting the effective cleavage of GPR65 mRNA substrate (Fig. 2H). These results indicated that the biomimetic Fe^{3+} metal-phenolic network was successful assembled.

2.2. Dual gene regulation of DR-TF@E in vitro

Under the premise of detecting cytotoxicity of TF@E on B16F10 melanoma cells, 50μg mL^{-1} of nanosystem was selected for the subsequent experiments (Figure S13). As designed in this study, the DR-TF@E nanosystem released DNAzyme system in cytoplasm for GPR65 gene silencing and Cas9 RNP in nucleus for GPX4 gene editing (Fig. 3A). Thus, prior to the evaluation of DNAzyme gene silencing and Cas9 RNP gene editing, whether the internalization and endosomal escape of DR-TF@E and the nuclear entry of Cas9 RNP was first confirmed. FAM-labeled

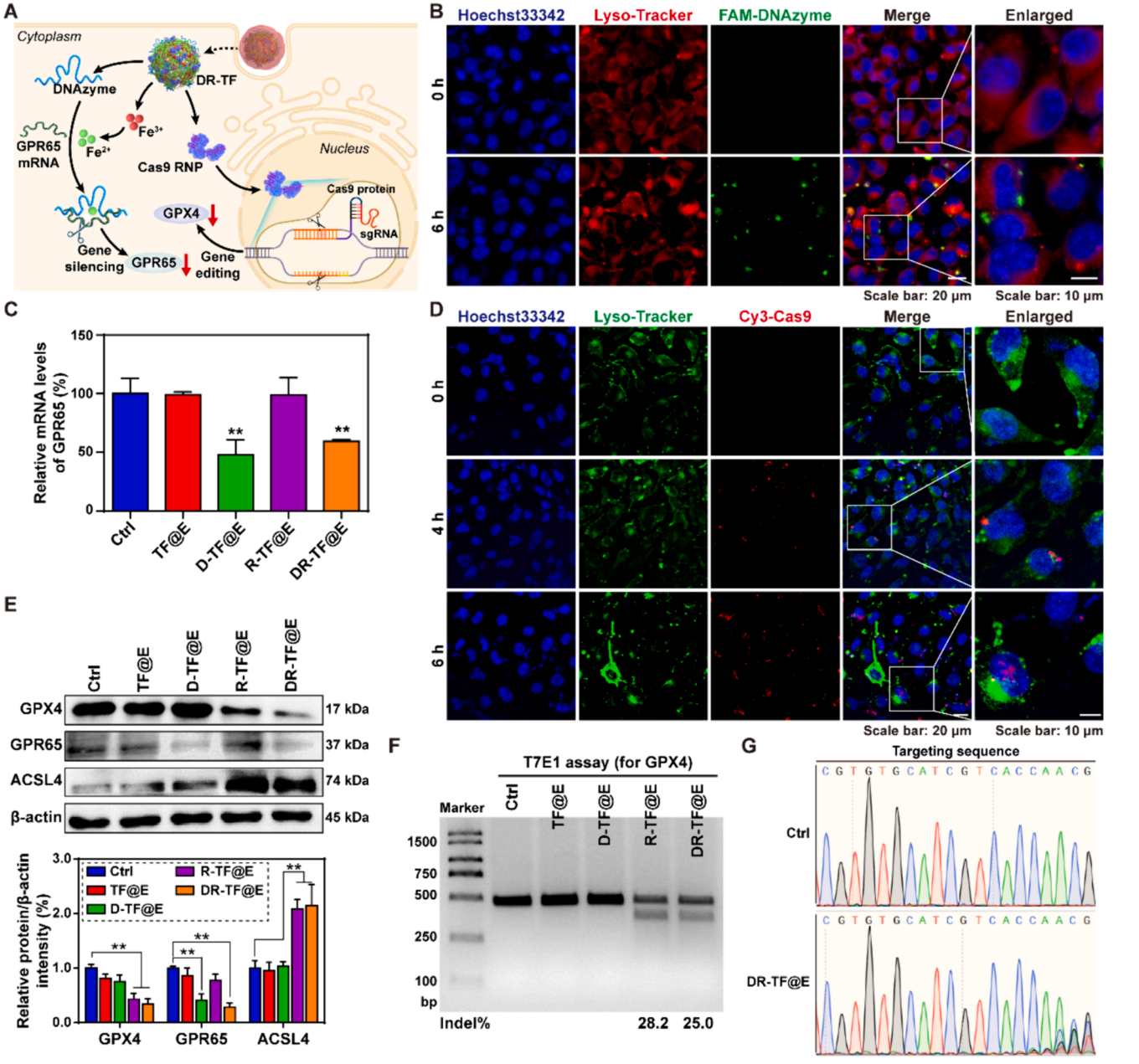

Fig. 3. Gene regulation efficiency of DR-TF@E nanosystem in vitro. A) Mechanism diagram of DR-TF@E released Cas9 RNP and DNAzyme for GPX4 gene editing and GPR65 gene silencing, respectively. B) The lysosome escape capacity of DR-TF@E nanosystem was detected by using FAM-labeled DNAzyme and representative images were taken by CLSM at different time periods (0 h, 6 h). Scale bar: 20 μm, enlarged scale bar: 10 μm. C) qRT-PCR analysis of GPR65 mRNA levels in B16F10 cells with different treatments. D) Cy3-labeled Cas9 protein assembled DR-TF@E was used to detect the lysosome escape and nuclear entry ability of Cas9 RNP. Scale bar: 20 μm, enlarged scale bar: 10 μm. E) Western blot analysis and quantitative analysis of GPX4, GPR65 and ACSL4 protein expression in B16F10 cells after treated with different formulations. F) T7E1 assay for GPX4 gene in B16F10 cells after different treatments. G) DNA sequencing data of GPX4 gene in B16F10 cells after treatment of DR-TF@E nanosystem. Data were expressed as means ± SD (n = 3). $^{**}P < 0.01$.

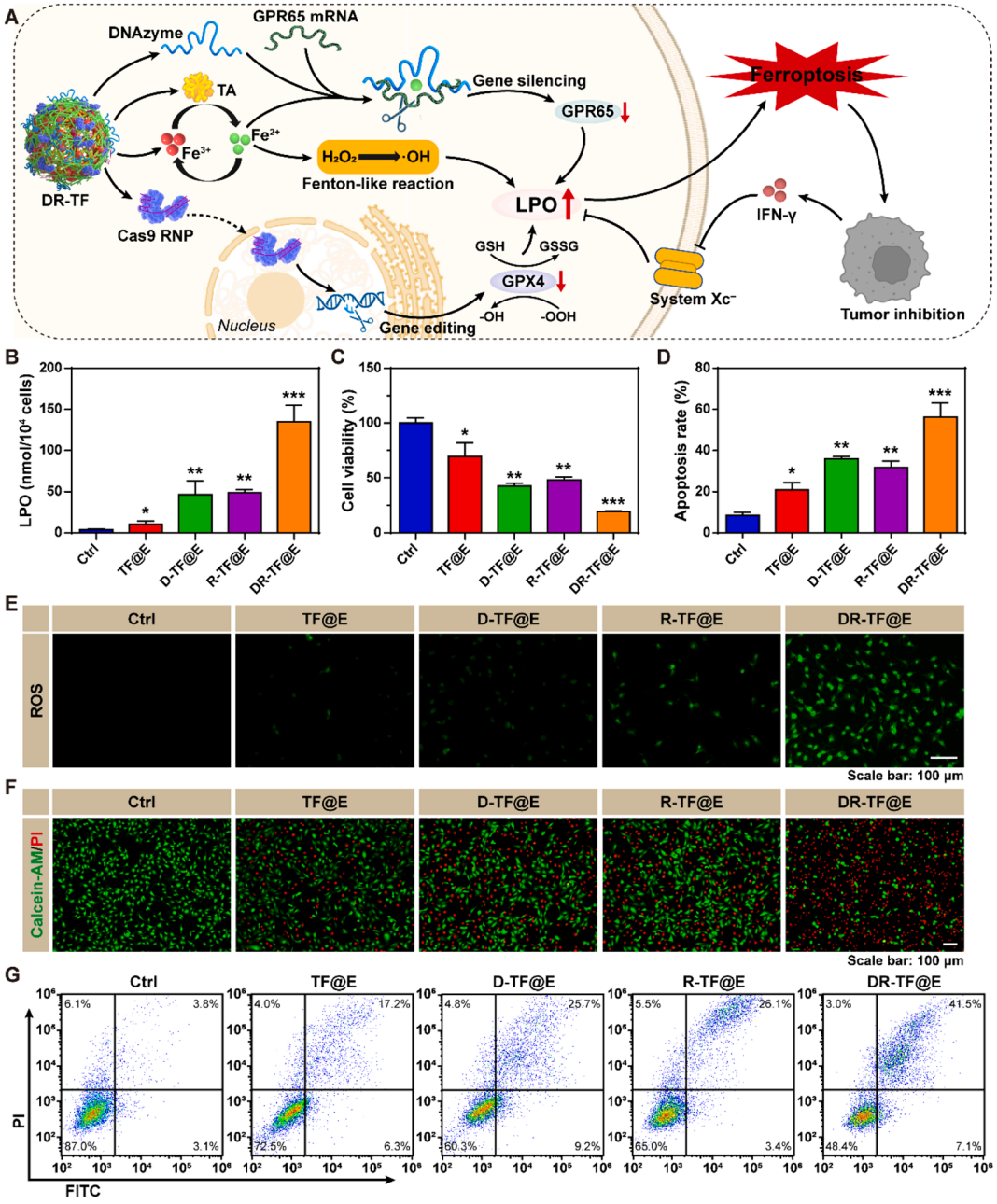

Fig. 4. Antitumor efficiency evaluation of DR-TF@E nanosystem in vitro. A) Schematic diagram of DR-TF@E nanosystem synergistic induced ferroptosis to realize tumor inhibition. B) Analysis of LPO content in B16F10 cells with different treatments. C) Cell viability analysis of B16F10 cells after treated with different formulations. D, G) Flow cytometry analysis of apoptosis in B16F10 cells. E) ROS fluorescence images of B16F10 cells stained with DCFH-DA. Scale bar: 100 μm. F) Representative fluorescence images of Calcein-AM (green, live cells) and PI (red, dead cells) co-stained B16F10 cells after treated with different formulations. Scale bar: 100 μm. Data were expressed as means ± SD (n = 3). $^{*}P < 0.05$, $^{**}P < 0.01$ and $^{***}P < 0.001$. (For interpretation of the references to colour in this figure legend, the reader is referred to the web version of this article.)

DNAzyme and lysosomal dyes of Lyso-Tracker were employed and found that the DNAzyme released from DR-TF@E could successfully escape through lysosomes into cytoplasm (Fig. 3B), which presumably due to the proton effects of metal cations. The gene silencing efficiency of DR-TF@E nanosystem was detected using qRT-PCR, and the D-TF@E and DR-TF@E groups could obviously downregulate the mRNA levels of GPR65, compared with the control and other groups (Fig. 3C). Moreover, Cy3-labeled Cas9 nuclease was used to monitor the nuclear entry of Cas9 RNP and it was shown that the significant Cy3 fluorescence signals were observed in the nucleus after 6 h of incubation under CLSM imaging (Fig. 3D), suggesting the successful endosomal escape and nuclear delivery of Cas9 RNP in B16F10 cells.

After verified the successful intracellular delivery, the gene regulation efficiency of DR-TF@E nanosystem was further studied. The results of Western blotting indicated that the DR-TF@E and R-TF@E treated groups could significantly decrease the protein expression of GPX4 rather than that of the control and other groups, and the protein levels of GPR65 could be obvious downregulated by the DR-TF@E and D-TF@E treatments (Fig. 3E), which consisted with the qRT-PCR results of Fig. 3C, and suggested the favorable gene regulation capacity of DR-TF@E nanosystem. To further verified the gene editing efficiency of DR-TF@E, a T7 Endonuclease I (T7E1) assay was performed to assess the frequency of mutation generated in B16F10 cells. The results indicated that the R-TF@E and DR-TF@E groups could lead to a much higher

mutation frequency of 28.2 % and 25.0 %, respectively (Fig. 3F and Figure S14). In addition, small insertions and deletions (indels) susceptible to double-strand breaks repair by the nonhomologous end joining were observed at the target site near the protospacer adjacent motif (PAM), through sequencing the PCR amplicons (Fig. 3G). The results suggested that the DR-TF@E nanosystem proposed the favorable dual-gene regulation capacity in vitro.

2.3. Ferroptosis induction and tumor inhibition of DR-TF@E in vitro

DR-TF@E nanosystem achieved the synergistic ferroptosis through dual-gene regulation of GPR65 and GPX4, which ultimately resulted in tumor inhibition (Fig. 4A). To detect the ferroptosis induced by nanosystem, lipid peroxidation (LPO), a key indicator of ferroptosis was investigated, and it was found that significant accumulation of LPO was observed in the D-TF@E, R-TF@E, and DR-TF@E groups, especially for DR-TF@E treated group (Fig. 4B). Subsequently, a DCFH-DA probe was used to determine the production of ROS, and the most pronounced intracellular fluorescence was observed in the DR-TF@E treated group compared to the other groups (Fig. 4E and Figure S15), and the fluorescence intensity of ROS was gradually enhanced with the increasing incubation time (Figure S16). To further verify the ferroptosis induction,

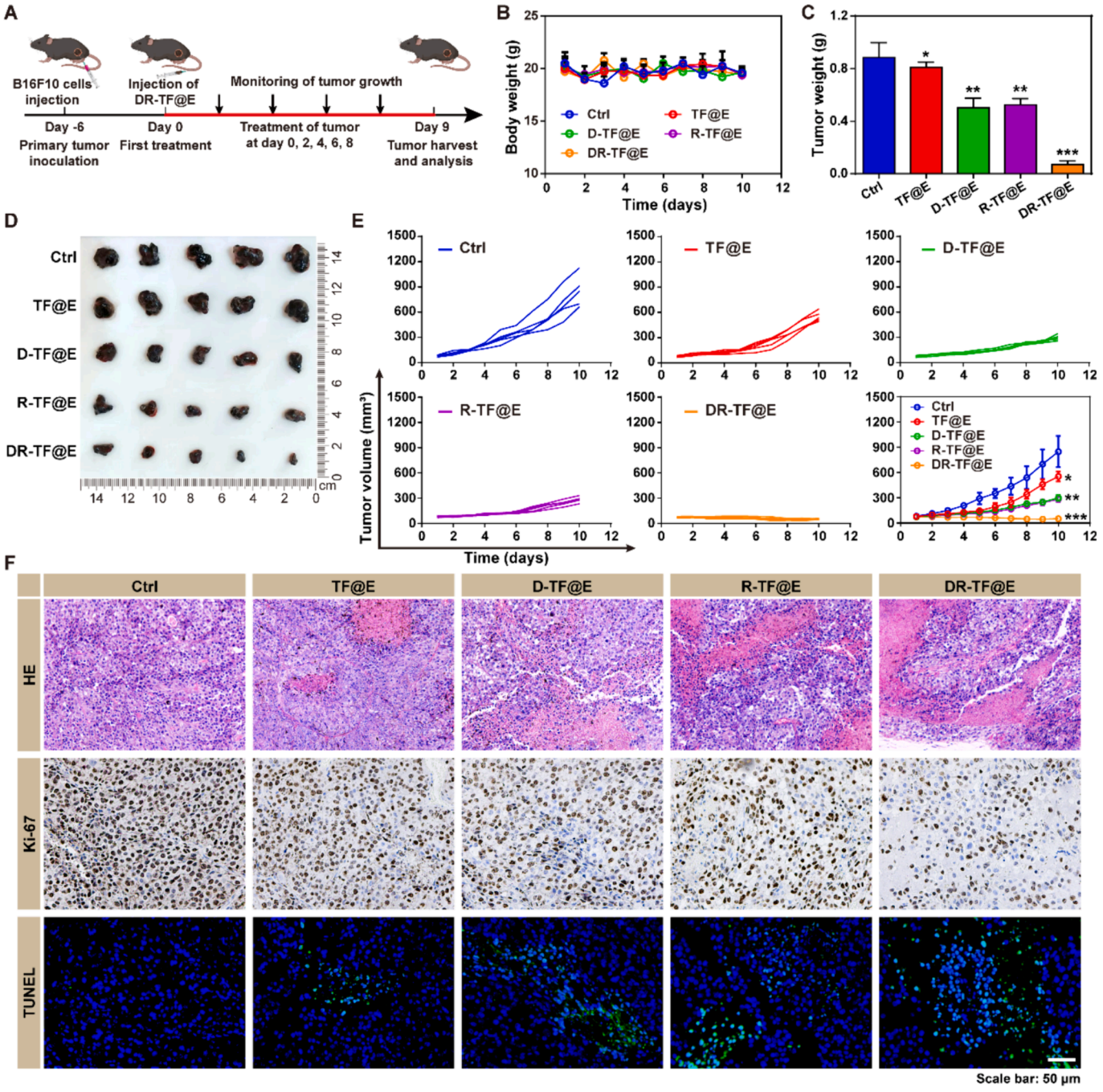

Fig. 5. Antitumor ability evaluation of DR-TF@E nanosystem in vivo. A) Schematic diagram of DR-TF@E nanosystem for orthotopic tumor administration. B) Body weight monitoring of mice during the treatment process. C) Tumor weight and D) physical images of excised tumors after different treatments as indicated. E) Tumor growth curves of mice in different treatment groups. F) Representative H&E staining, IHC analysis of Ki-67 and TUNEL fluorescent staining in tumor sections. Scale bar: 50 μm. Data were expressed as means ± SD (n = 5). $^{*}P < 0.05$, $^{**}P < 0.01$ and $^{***}P < 0.001$.

the protein expression of crucial ferroptosis-related gene, GPX4 and ACSL4, were detected using Western blotting. As shown in Fig. 3E, the DR-TF@E group could obviously decrease the protein level of GPX4 and increase the protein expression of ASCL4 compared with the other groups, suggesting that the DR-TF@E could induce ferroptosis through interfering with the related genes.

Subsequently, the performance of DR-TF@E nanosystem on tumor cells viability were performed. As shown in MTS assay detection, DR-TF@E nanosystem exhibited the highest cytotoxicity to B16F10 cells compared with other treatment groups (Fig. 4C). The live/dead fluorescent cell staining assay using the Calcein-AM and PI dyes indicated that the DR-TF@E treated groups showed the weakest green intensity and the highest red intensity compared to the other treated groups (Fig. 4F), which consistent with the trend of MTS results. Additionally, the cell apoptosis induced by nanosystem was measured using flow cytometry, and the highest apoptosis rate was observed in the DR-TF@E group, compared with the PBS and others TF@E-based nanosystem groups (Fig. 4D, G). In summary, the above results revealed that the DR-TF@E nanosystem could induce ferroptosis and thus resulted in tumor cell inhibition.

2.4. Antitumor effects of DR-TF@E nanosystem in vivo

The favorable in vivo therapeutic effect and lower biological toxicity are based on the excellent tumor targeting capacity of nanosystem. Thus, the biodistribution of DR-TF@E in orthotopic xenograft mice after systematic administration was detected and it was observed that the indocyanine green (ICG)-assembled DR-TF@E was mainly accumulated in the tumor regions under IVIS imaging, and further confirmed by the fluorescence signals distribution in subsequently harvested major organs (i.e., heart, liver, spleen, kidney, and lung) and tumor tissues (Figure S17), suggesting the favorable tumor targeting of nanosystem. Encouraged by the positive results of in vitro experiments, the antitumor efficacy of synthetic nanosystem was proceed on B16F10 orthotopic tumor model, and the nanosystems were first administrated via intravenous injection when the tumor volume of about 80 mm^3 (Fig. 5A). The changes of mouse weight were monitored and no lethality or pronounced drop was observed in the treatment process (Fig. 5B). The tumor growth curve was monitored and found that the DR-TF@E groups (51.3 ± 7.5 mm^3) exhibited the most robust suppression of tumor growth, compared with the PBS (848.2 ± 185.1 mm^3), TF@E (552.8 ± 58.4 mm^3), D-TF@E (298.3 ± 32.3 mm^3), and R-TF@E (283.3 ± 34.9 mm^3) treated groups (Fig. 5E), indicating the superior antitumor efficacy of nanosystem. In addition, the xenograft tissues were harvested and weighed after euthanasia of mice, and the trend of physical image and weight of collected tumor further confirmed the therapeutic efficacy of nanosystems in vivo (Fig. 5C-D).

The Hematoxylin-eosin (H&E) and immunohistochemistry (IHC) staining were performed on the tumor sections of each group for further evaluate the therapeutic effects of DR-TF@E nanosystem. The H&E staining results showed that the TF@E based nanosystem treated groups exhibited an obvious decreased cell density, especially for the DR-TF@E group (Fig. 5F). IHC staining of Ki-67 for cell proliferation and TUNEL (terminal deoxynucleotidyl transferase-mediated deoxyuridine triphosphate nick end labeling) staining for cell apoptosis indicated that the most proliferation repression and apoptosis promotion effects induced by the DR-TF@E treatment (Fig. 5F). Furthermore, H&E staining of the major organs of all groups demonstrated that no noticeable abnormality or appreciable organ damage (Figure S18). The harvested peripheral blood of mice with treatment of PBS or DR-TF@E nanosystem, and the separated serum was used for the standard serum biochemistry analysis. The results showed that the value of liver and kidney function indicators, such as, ALT (alanine aminotransferase), ALP (alkaline phase), AST (aspartate aminotransferase), TP (total protein), UREA (urea), and CREA (creatinine), were within the normal reference range both in the PBS and nanosystem groups (Figure S19A–F), suggesting the favorable biocompatibility of nanosystem in vivo. In all, the DR-TF@E nanosystem emerged robust antitumor efficiency with highly biological safety in vivo.

2.5. Gene interference and ferroptosis induction of DR-TF@E in vivo

The efficiency of GPX4 gene editing and GPR65 gene silencing induced by DR-TF@E were further verified in the tumor tissues. Western blotting results revealed that the DR-TF@E and R-TF@E treatments could obviously downregulate the protein levels of GPX4, and the protein expression of GPR65 was significantly decreased by the D-TF@E and DR-TF@E treated groups (Fig. 6A-B), demonstrating the excellent gene interference capacity of nanosystem. In order to further confirmed the GPX4 gene editing efficiency of DR-TF@E, a T7E1 mismatch detection assay was also performed in the tumor tissues and indicated that the R-TF@E and DR-TF@E groups showed the mutations frequency of 21.1 % and 19.3 %, respectively (Fig. 6C and Figure S20). To more fully reveal the results of gene editing, Sanger gene sequencing was employed and revealed that the DR-TF@E treatment induced the small insertions and deletions (indels) on the targeting DNA sequences (Fig. 6D).

In view of ferroptosis induction of the DR-TF@E, ferroptosis related crucial genes, GPX4, GPR65 and ASCL4, were evaluated in the tumor tissues by western blotting and the results demonstrated that the DR-TF@E group could significantly decrease the protein levels of GPX4 and GPR65, and increased the protein expression of ACSL4 (Fig. 6A). In addition, IHC staining of GPX4, GPR65, and ACSL4 in the tumor sections showed and verified that the DR-TF@E treatment could downregulate the protein levels of GPX4 and GPR65 and upregulate the protein expression of ACSL4 (Fig. 6E and Figure S21), which suggesting the efficient ferroptosis induction of the DR-TF@E in vivo.

2.6. Robust antitumor immunity and pulmonary metastasis of DR-TF@E in vivo

To elucidate the DR-TF@E mediated tumor ferroptosis-immune response, the tumor and spleen tissues of all treatment groups were collected and analyzed using flow cytometry. As crucial antigen-presenting cells in initiating immunity, matured dendritic cells (DCs, $CD11c^+CD80^+CD86^+$) were first evaluated in tumors and the results showed that the DR-TF@E treatment could significantly promote the maturation of DCs (22.9 ± 1.2 %) compared with PBS treated group (8.1 ± 1.1 %) (Fig. 7A and B). Subsequently, the percentage of infiltrated cytotoxic T lymphocytes (CTLs, $CD3^+CD4^-CD8^+$) were identified in spleens, and the percentage of $CD8^+$ T cells in the DR-TF@E treated group (23.1 ± 3.6 %) was higher than those in the PBS group (13.2 ± 0.5 %) (Fig. 7C-D). Meanwhile, the $CD4^+$ helper T cells were evaluated in spleens and found that the DR-TF@E treatment could obviously upregulate the population of $CD4^+$ T cells (43.5 ± 1.7 %) compared with the PBS administration (29.6 ± 0.9 %) (Fig. 7C-D). Meanwhile, immunofluorescence staining of CD8 and CD4 in tumor sections indicated that the DR-TF@E nanosystem treatment could significantly increase the CTLs and helper T cells infiltration compared with PBS administration, which was similar to the results of flow cytometry (Figure S22). In addition, the serum levels of interferon-gamma (IFN-γ), interleukin-6 (IL-6), and tumor necrosis factor-α (TNF-α) were detected to further confirmed the antitumor immunity. It was indicated that the DR-TF@E treatment could significantly increase the levels of IFN-γ, IL-6 and TNF-α compared with the PBS treatment (Fig. 7E-G). The IFN-γ-System Xc^- pathway in ferroptosis was also confirmed by evaluating the crucial component of System Xc^-, SLC7A11. The results of SLC7A11 protein expression in tumor sections was detected by western blotting, and indicated that the DR-TF@E could significant downregulate the SLC7A11 protein level, compared with the PBS group (Figure S23), which suggested that the DR-TF@E nanosystem could further promote ferroptosis by inducing tumor cell to secrete IFN-γ, thereby inhibiting

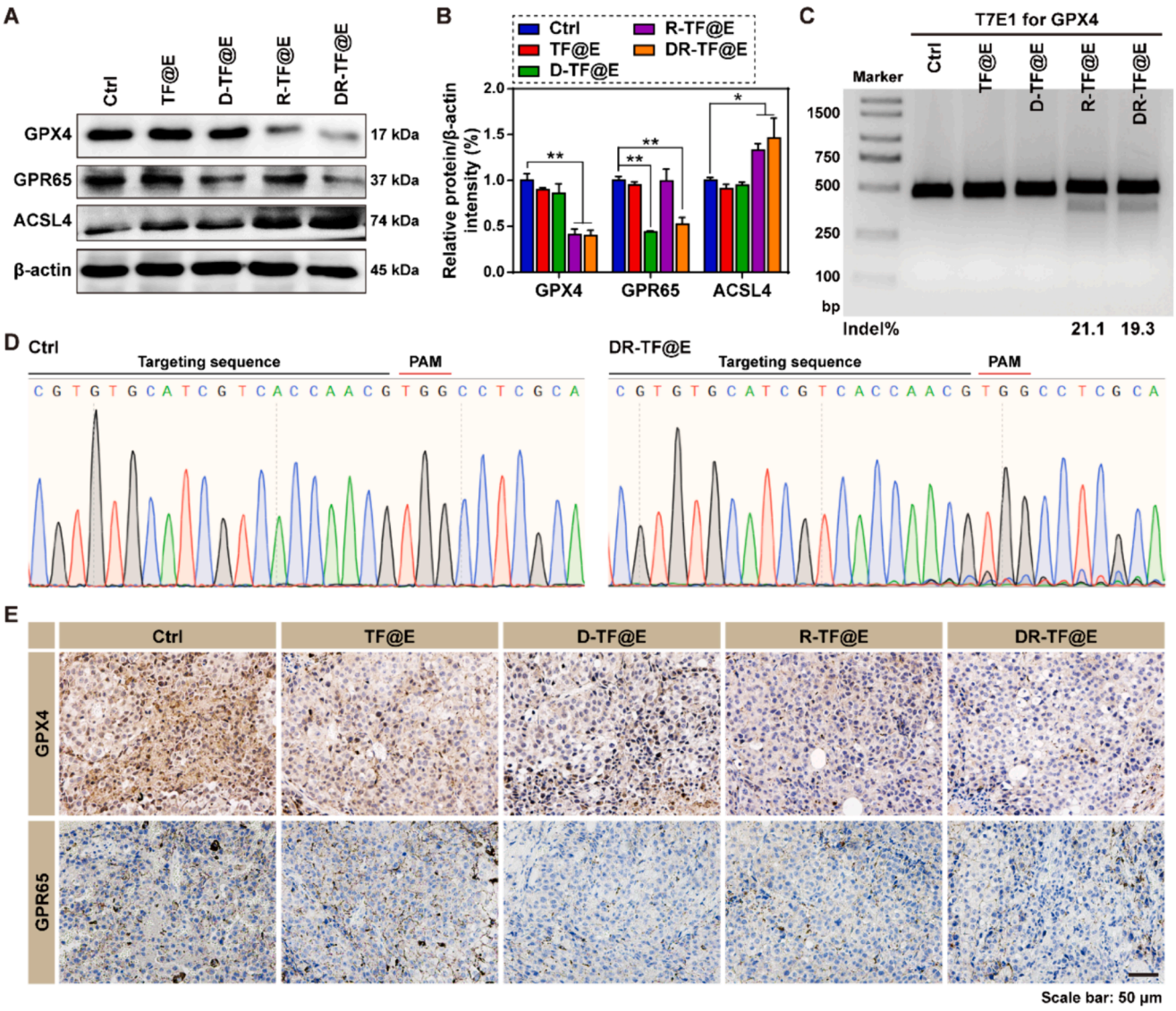

Fig. 6. Effectiveness evaluation of gene regulation and ferroptosis induction by DR-TF@E in vivo. A-B) Western blot and corresponding quantitative analysis of GPX4, GPR65 and ACSL4 protein expression in tumor tissues treated with different formulations. C) T7E1 assay for GPX4 in tumor tissues. D) DNA sequencing data of GPX4 gene in tumor tissues with different treatments. E) IHC staining of GPX4 and GPR65 in tumor sections. Scale bar: 50 μm. Data were expressed as means ± SD (n = 5). $^{*}P < 0.05$, $^{**}P < 0.01$.

the System Xc^{-} pathway. In summary, this nanosystem reversed immunosuppressed "cold" tumors to immunoactivated "hot" tumors and implemented robust tumor ferroptosis-immunotherapy.

The capacity of DR-TF@E nanosystem on metastatic tumor was further verified, and the pulmonary metastatic tumor model was established by intravenous injection of B16F10 cells. Lung tissues from each treatment groups were collected at the end of the experiment for detailed analysis and evaluation (Fig. 7H). In contrast to the PBS treated group covering dark metastatic tumor nodules, the invisible metastatic tumor nodules were observed on the surface of lung in the DR-TF@E treated group, which was similar to the unmodeled group. Notably, only a small amount of metastatic tumor nodules was observed on the lungs of D-TF@E and R-TF@E treatment groups (Fig. 7I), suggesting the inhibition of synergistic ferroptosis-immunotherapy on metastatic tumor. To further verified the anti-metastatic tumor efficiency of nanosystem, the lung tissues of each treatment group were performed H&E staining. H&E staining of lung tissues results indicated that a barely visible metastatic tumor nodules were observed on the lung tissue sections after DR-TF@E treatment, which was consisted with the physic images of lung tissues (Fig. 7J). These findings provided that the DR-TF@E nanosystem proposed a powerful anti-metastatic tumor efficiency.

3. Conclusions

Summarily, we successfully developed EM-based biomimetic Fe^{3+} metal-phenolic networks to realize synergistic tumor ferroptosis-immunotherapy through simultaneous delivery of DNAzyme and Cas9 RNP systems. The biomimetic DR-TF@E nanosystem could precision delivery of Cas9 RNP and DNAzyme systems for GPX4 gene editing and GPR65 gene silencing. To be specific, Fe^{3+} released from nanosystem was reduced to Fe^{2+} by TA in the TME, which assisted in endosomal escape of nanosystem and served as the metal cofactor of DNAzyme system for GPR65 gene silencing. Meanwhile, Fe^{2+} interacted with H_2O_2 initiated the Fenton-like reaction and Cas9 RNP mediated gene editing of GPX4 induced the enhanced ferroptosis. The ferroptosis induced immunogenic cell death-initiated a series of systemic immune responses and eventually resulted in tumor elimination. This biomimetic nanosystem achieves dual-gene regulation with highly efficiency and biosafety and provides a robust synergistic tumor ferroptosis-

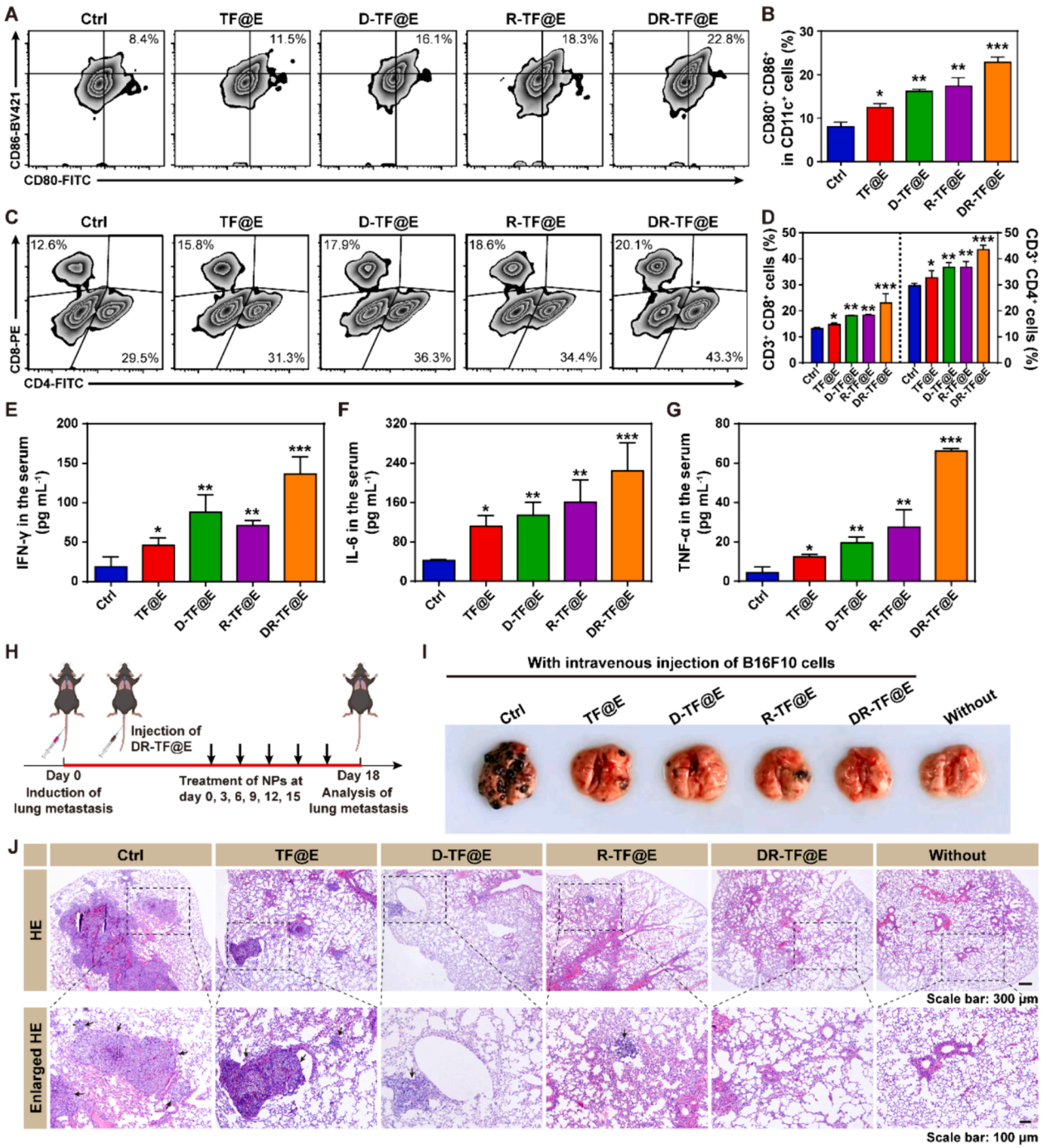

Fig. 7. Evaluation of antitumor immune effects and pulmonary metastasis inhibition by DR-TF@E nanosystem in vivo. A-B) Flow cytometry and quantitative analysis of matured DCs ($CD80^+CD86^+$ gated on $CD11c^+$ cells) in tumor tissues. C-D) Flow cytometry analysis of $CD4^+$ and $CD8^+$ T cells (gated on $CD3^+$ T cells) in spleen tissues. The expression levels of E) IFN-γ, F) IL-6 and G) TNF-α in serum were detected by ELISA assay. H) Schematic illustration of DR-TF@E nanosystem for pulmonary metastasis inhibition. I) Representative physical images of excised lung tissues treated with different formulations. J) H&E staining of metastatic tumor nodules in lung. The black arrow in enlarged H&E staining indicates the metastatic tumor nodules. Scale bar: 300 μm. Enlarged scale bar: 100 μm. Data were expressed as means ± SD (n = 5). $^*P < 0.05$, $^{**}P < 0.01$ and $^{***}P < 0.001$.

immunotherapy.

4. Materials and Methods

4.1. Materials

Ferric chloride hexahydrate ($FeCl_3{\cdot}6H_2O$) and tannic acid (TA) were acquired from McLean Biochemical Co., Ltd. (Shanghai, China). Polyallylamine hydrochloride (PAH) was purchased from Sinopharm Chemical Reagent Co., Ltd. (Shanghai, China). DMEM culture medium, MTS detection kit were obtained from KeyGen Biotech. Co., Ltd. (Nanjing, China). Serum-free cell cryopreservation solution was purchased from New Cell & Molecular Biotech Co., Ltd. (Suzhou, China). Lipid Peroxide (LPO) Content Assay Kit was purchased from Beijing Solarbio Science & Technology Co., Ltd. (Beijing, China). Both of the FastPure® Cell/Tissue DNA/Total RNA Isolation Kit V2, T7 Endonuclease I, HiScript III RT SuperMix for qPCR (+gDNA wiper), and ChamQ Universal SYBR qPCR Master Mix were purchased from Vazyme

Biotechnology Co., Ltd. (Nanjing, China). ELISA kits for TNF-α, IFN-γ and IL-6 analysis were obtained from Dakewe Bio-engineering Co., Ltd. (Shenzhen, China). All aqueous solutions were prepared using ultrapure water (18.2 MU, Milli-Q; Millipore). The primary antibodies were commercially available and listed in Table S1. All oligonucleotides were obtained from Sangon Biotech (Shanghai) Co., Ltd. (Shanghai China) and the sequences were provided in Table S2 and S3.

4.2. Biodistribution and anti-tumor evaluation

All animal procedures were performed under the guidance of the Institutional Animal Care and Use Committee of the Nanjing University of Chinese Medicine (ethical approval number: 202309A042).

For orthotopic tumor model, melanoma B16F10 cells (1×10^6 cells) were injected subcutaneously into the right flank of C57BL/6 mice. The modeled mice were randomly divided into five groups when the tumor size was about 80 mm^3, which treated with PBS, TF@E, D-TF@E, R-TF@E and DR-TF@E through intravenous injection every other day for ten days, respectively. the mice body weight and tumor volume were monitored at the treatment process, and the tumor volume was calculated using the following formula: $V_{tumor} = 1/2 \times (length \times width^2)$. At the end of experiment, the mice were sacrificed and tumor tissues, peripheral blood, and major organs were collected for further analysis. To further verified the antitumor immune-responses of DR-TF@E nanosystems, the population of $CD11c^+CD86^+CD80^+$ DCs, $CD3^+CD8^+$ infiltrated cytotoxic T cells, and $CD3^+CD4^+$ helper T cells in tumor or spleen tissues were analyzed by flow cytometry.

For pulmonary metastases tumor model, the mice were intravenous injection of melanoma B16F10 cells (1×10^5 cells) and randomly divided into five groups. The modeled mice were administrated with nanosystem every two days for 15 days. At the end of experiment, the mice were sacrificed and the pulmonary tissues were harvested and photographed. The pulmonary metastasis of tumor was visualized by H&E staining and the metastasis regions were marked in the pulmonary sections of each group to evaluate the anti-metastasis efficiency of nanosystem.

4.3. Statistical analysis

At least three experiments were carried out in duplicate, and the experimental data were expressed in the form of means ± standard deviation. For statistical significance between two groups verified using a two-sided Student's *t* test analysis. $^*P < 0.05$, $^{**}P < 0.01$ or $^{***}P < 0.001$ means statistical significance.

CRediT authorship contribution statement

Chao Chen: Writing – review & editing, Writing – original draft, Supervision, Project administration, Methodology, Investigation, Funding acquisition, Conceptualization. **Xueting Shen:** Writing – original draft, Visualization, Validation, Software, Methodology, Investigation. **Silin Shi:** Methodology, Investigation. **Yin Xu:** Writing – original draft, Data curation. **Hongxiu Song:** Software. **Lihua Qu:** Software. **Shiyu Du:** Software, Data curation. **Yamei Gao:** Investigation. **Xin Han:** Writing – review & editing, Writing – original draft, Supervision, Funding acquisition, Conceptualization.

Declaration of competing interest

The authors declare that they have no known competing financial interests or personal relationships that could have appeared to influence the work reported in this paper.

Data availability

Data will be made available on request.

Acknowledgments

This work was supported by the National Natural Science Foundation of China (82302365); Supporting Project of Nanjing University of Chinese Medicine to NSFC (XPT82302365); Yangtze River Delta joint sci-tech innovation and research projects (2023CSJZN0600); the Priority Academic Program Development of Jiangsu Higher Education Institutions (Integration of Chinese and Western Medicine); Jiangsu Key Discipline Construction Fund of the 14th Five-Year Plan (Biology); the Natural Science Foundation of Hubei Province, China (2024AFB517); the Natural Science Foundation of the Higher Education Institutions of Jiangsu Province, China (23KJB310015); the National College Student Innovation Training Program (202410315031Z); the Graduate Research & Practice Innovation Program of Jiangsu Province (SJCX23_0845 and KYCX23_2069).

Author Contributions

C.C., X.S. and L.Q. performed the nanosystem synthesized and characterized. C.C., X.S., S.D. and Y.G. assisted in in vitro experiments. X.S., C.C., S.S. Y.X. and H.S. performed the in vivo animal evaluation. C. C., X.S. and X.H. wrote the manuscript with feedback from all the authors. C.C. and X.H. conceived the idea, designed the experiments, and supervised the project.

Appendix A. Supplementary data

Supplementary data to this article can be found online at https://doi.org/10.1016/j.cej.2024.156050.

References

[1] Y. Xie, W. Hou, X. Song, Y. Yu, J. Huang, X. Sun, R. Kang, D. Tang, Ferroptosis: process and function, Cell Death Differ 23 (3) (2016) 369–379, https://doi.org/10.1038/cdd.2015.158.
[2] C. Liang, X. Zhang, M. Yang, X. Dong, Recent Progress in Ferroptosis Inducers for Cancer Therapy, Adv Mater 31 (51) (2019) e1904197.
[3] J. Wang, Z. Fang, C. Zhao, Z. Sun, S. Gao, B. Zhang, D. Qiu, M. Yang, F. Sheng, S. Gao, Y. Hou, Intelligent Size-Switchable Iron Carbide-Based Nanocapsules with Cascade Delivery Capacity for Hyperthermia-Enhanced Deep Tumor Ferroptosis, Adv Mater 36 (9) (2024) e2307006.
[4] J. Diao, Y. Jia, E. Dai, J. Liu, R. Kang, D. Tang, L. Han, Y. Zhong, L. Meng, Ferroptotic therapy in cancer: benefits, side effects, and risks, Mol Cancer 23 (1) (2024) 89, https://doi.org/10.1186/s12943-024-01999-9.
[5] D. Liang, Y. Feng, F. Zandkarimi, H. Wang, Z. Zhang, J. Kim, Y. Cai, W. Gu, B. R. Stockwell, X. Jiang, Ferroptosis surveillance independent of GPX4 and differentially regulated by sex hormones, Cell 186 (13) (2023) 2748–2764 e22, https://doi.org/10.1016/j.cell.2023.05.003.
[6] K. Bersuker, J.M. Hendricks, Z. Li, L. Magtanong, B. Ford, P.H. Tang, M.A. Roberts, B. Tong, T.J. Maimone, R. Zoncu, M.C. Bassik, D.K. Nomura, S.J. Dixon, J. A. Olzmann, The CoQ oxidoreductase FSP1 acts parallel to GPX4 to inhibit ferroptosis, Nature 575 (7784) (2019) 688–692, https://doi.org/10.1038/s41586-019-1705-2.
[7] H. Kalkavan, M.J. Chen, J.C. Crawford, G. Quarato, P. Fitzgerald, S.W.G. Tait, C. R. Goding, D.R. Green, Sublethal cytochrome c release generates drug-tolerant persister cells, Cell 185 (18) (2022) 3356–3374 e22, https://doi.org/10.1016/j.cell.2022.07.025.
[8] I. Ingold, C. Berndt, S. Schmitt, S. Doll, G. Poschmann, K. Buday, A. Roveri, X. Peng, F. Porto Freitas, T. Seibt, L. Mehr, M. Aichler, A. Walch, D. Lamp, M. Jastroch, S. Miyamoto, W. Wurst, F. Ursini, E.S.J. Arner, N. Fradejas-Villar, U. Schweizer, H. Zischka, J.P. Friedmann Angeli, M. Conrad, Selenium Utilization by GPX4 Is Required to Prevent Hydroperoxide-Induced Ferroptosis, Cell 172 (3) (2018) 409–422 e21, https://doi.org/10.1016/j.cell.2017.11.048.
[9] H. Alborzinia, A.F. Florez, S. Kreth, L.M. Bruckner, U. Yildiz, M. Gartlgruber, D. I. Odoni, G. Poschet, K. Garbowicz, C. Shao, C. Klein, J. Meier, P. Zeisberger, M. Nadler-Holly, M. Ziehm, F. Paul, J. Burhenne, E. Bell, M. Shaikhkarami, R. Wurth, S.A. Stainczyk, E.M. Wecht, J. Kreth, M. Buttner, N. Ishaque, M. Schlesner, B. Nicke, C. Stresemann, M. Llamazares-Prada, J.H. Reiling, M. Fischer, I. Amit, M. Selbach, C. Herrmann, S. Wolfl, K.O. Henrich, T. Hofer, A. Trumpp, F. Westermann, MYCN mediates cysteine addiction and sensitizes neuroblastoma to ferroptosis, Nat Cancer 3 (4) (2022) 471–485, https://doi.org/10.1038/s43018-022-00355-4.
[10] W. Zhang, Y. Liu, Y. Liao, C. Zhu, Z. Zou, GPX4, ferroptosis, and diseases, Biomed Pharmacother 174 (2024) 116512, https://doi.org/10.1016/j.biopha.2024.116512.

[11] R. Kong, N. Wang, W. Han, W. Bao, J. Lu, IFNgamma-mediated repression of system xc(-) drives vulnerability to induced ferroptosis in hepatocellular carcinoma cells, J Leukoc Biol 110 (2) (2021) 301–314, https://doi.org/10.1002/JLB.3MA1220-815RRR.
[12] F. Zhao, H. Yu, L. Liang, C. Wang, D. Shi, X. Zhang, Y. Ying, W. Cai, W. Li, J. Li, J. Zheng, L. Qiao, S. Che, J. Yu, Redox Homeostasis Disruptors Based on Metal-Phenolic Network Nanoparticles for Chemo/Chemodynamic Synergistic Tumor Therapy through Activating Apoptosis and Cuproptosis, Adv Healthc Mater 12 (29) (2023) e2301346.
[13] C.J. Kim, F. Ercole, J. Chen, S. Pan, Y. Ju, J.F. Quinn, F. Caruso, Macromolecular Engineering of Thermoresponsive Metal-Phenolic Networks, J Am Chem Soc 144 (1) (2022) 503–514, https://doi.org/10.1021/jacs.1c10979.
[14] L. Jiang, Y. Zeng, H. Li, Z. Lin, H. Liu, J.J. Richardson, Z. Gao, D. Wu, L. Liu, F. Caruso, J. Zhou, Peptide-Based Coacervate Protocells with Cytoprotective Metal-Phenolic Network Membranes, J Am Chem Soc 145 (44) (2023) 24108–24115, https://doi.org/10.1021/jacs.3c07748.
[15] L. Xie, J. Li, G. Wang, W. Sang, M. Xu, W. Li, J. Yan, B. Li, Z. Zhang, Q. Zhao, Z. Yuan, Q. Fan, Y. Dai, Phototheranostic Metal-Phenolic Networks with Antiexosomal PD-L1 Enhanced Ferroptosis for Synergistic Immunotherapy, J Am Chem Soc 144 (2) (2022) 787–797, https://doi.org/10.1021/jacs.1c09753.
[16] T. Liu, M. Zhang, W. Liu, X. Zeng, X. Song, X. Yang, X. Zhang, J. Feng, Metal Ion/Tannic Acid Assembly as a Versatile Photothermal Platform in Engineering Multimodal Nanotheranostics for Advanced Applications, ACS Nano 12 (4) (2018) 3917–3927, https://doi.org/10.1021/acsnano.8b01456.
[17] Z. Zhang, L. Xie, Y. Ju, Y. Dai, Recent Advances in Metal-Phenolic Networks for Cancer Theranostics, Small 17 (43) (2021) e2100314.
[18] Q. Zhang, R.H. Fang, W. Gao, L. Zhang, A Biomimetic Nanoparticle to "Lure and Kill" Phospholipase A2, Angew Chem Int Ed Engl 59 (26) (2020) 10461–10465, https://doi.org/10.1002/anie.202002782.
[19] Y.S. Lin, C.L. Haynes, Impacts of mesoporous silica nanoparticle size, pore ordering, and pore integrity on hemolytic activity, J Am Chem Soc 132 (13) (2010) 4834–4842, https://doi.org/10.1021/ja910846q.
[20] T. Yu, K. Wang, J. Wang, Y. Liu, T. Meng, F. Hu, H. Yuan, M-MDSCs mediated trans-BBB drug delivery for suppression of glioblastoma recurrence post-standard treatment, J Control Release 369 (2024) 199–214, https://doi.org/10.1016/j.jconrel.2024.03.043.
[21] J. Shi, W. Nie, X. Zhao, X. Yang, H. Cheng, T. Zhou, Y. Zhang, K. Zhang, J. Liu, An Intracellular Self-Assembly-Driven Uninterrupted ROS Generator Augments 5-Aminolevulinic-Acid-Based Tumor Therapy, Adv Mater 34 (30) (2022) e2201049.
[22] H.N. Bell, B.R. Stockwell, W. Zou, Ironing out the role of ferroptosis in immunity, Immunity 57 (5) (2024) 941–956, https://doi.org/10.1016/j.immuni.2024.03.019.
[23] C. Chen, S.Y. Du, Q.L. Lu, K.G. Liu, Y.C. Pan, Y.Q. Jiang, J.J. Yang, X. Han, Y. J. Song, Tumor-associated miRNAs activated HCR-DNAzyme theranostic nanosystem to trigger innate- and adaptive-immune responses for long-term immunotherapy, Chem Eng J 473 (2023) https://doi.org/ARTN 145192 1016/j.cej.2023.145192.
[24] C. Yang, M. Wang, M. Chang, M. Yuan, W. Zhang, J. Tan, B. Ding, P. Ma, J. Lin, Heterostructural Nanoadjuvant CuSe/CoSe(2) for Potentiating Ferroptosis and Photoimmunotherapy through Intratumoral Blocked Lactate Efflux, J Am Chem Soc 145 (13) (2023) 7205–7217, https://doi.org/10.1021/jacs.2c12772.
[25] M. Zhang, X. Jin, M. Gao, Y. Zhang, B.Z. Tang, A Self-Reporting Fluorescent Salicylaldehyde-Chlorambucil Conjugate as a Type-II ICD Inducer for Cancer Vaccines, Adv Mater 34 (36) (2022) e2205701.
[26] A.R. van Vliet, S. Martin, A.D. Garg, P. Agostinis, The PERKs of damage-associated molecular patterns mediating cancer immunogenicity: From sensor to the plasma membrane and beyond, Semin Cancer Biol 33 (2015) 74–85, https://doi.org/10.1016/j.semcancer.2015.03.010.
[27] C. Shi, M. Chen, X. Li, Y. Fu, D. Yang, T. Wen, W. Zhao, Y. Sun, W. Wang, C. Lu, Q. Wu, C. Wu, X. Pan, G. Quan, ATP-adenosine axis regulation combined with microneedle assisted photoimmunotherapy to boost the immunotherapy efficiency, J Control Release 367 (2024) 1–12, https://doi.org/10.1016/j.jconrel.2024.01.035.
[28] J. Li, Q. Zhao, N. Zhang, L. Wu, Q. Wang, J. Li, Q. Pan, Y. Pu, K. Luo, Z. Gu, B. He, Triune Nanomodulator Enables Exhausted Cytotoxic T Lymphocyte Rejuvenation for Cancer Epigenetic Immunotherapy, ACS Nano (2024), https://doi.org/10.1021/acsnano.4c02337.
[29] L. Galluzzi, E. Guilbaud, D. Schmidt, G. Kroemer, F.M. Marincola, Targeting immunogenic cell stress and death for cancer therapy, Nat Rev Drug Discov (2024), https://doi.org/10.1038/s41573-024-00920-9.
[30] Y. Huang, Y. Chen, S. Zhou, L. Chen, J. Wang, Y. Pei, M. Xu, J. Feng, T. Jiang, K. Liang, S. Liu, Q. Song, G. Jiang, X. Gu, Q. Zhang, X. Gao, J. Chen, Dual-mechanism based CTLs infiltration enhancement initiated by Nano-sapper potentiates immunotherapy against immune-excluded tumors, Nat Commun 11 (1) (2020) 622, https://doi.org/10.1038/s41467-020-14425-7.
[31] S. de Souza Ferreira, M.K. Bek, C.a., Tibbitt, pH sensing shapes immune cell function: The role of GPR65 and its implications for allergic disease, Allergy 78 (7) (2023) 2061–2063, https://doi.org/10.1111/all.15708.
[32] X. Chen, A. Jaiswal, Z. Costliow, P. Herbst, E.A. Creasey, N. Oshiro-Rapley, M. J. Daly, K.L. Carey, D.B. Graham, R.J. Xavier, pH sensing controls tissue inflammation by modulating cellular metabolism and endo-lysosomal function of immune cells, Nat Immunol 23 (7) (2022) 1063–1075, https://doi.org/10.1038/s41590-022-01231-0.
[33] D. Mori, T. Tsujikawa, Y. Sugiyama, S.I. Kotani, S. Fuse, G. Ohmura, A. Arai, T. Kawaguchi, S. Hirano, O. Mazda, T. Kishida, Extracellular acidity in tumor tissue upregulates programmed cell death protein 1 expression on tumor cells via proton-sensing G protein-coupled receptors, Int J Cancer 149 (12) (2021) 2116–2124, https://doi.org/10.1002/ijc.33786.
[34] C. Chen, Y. Ma, S. Du, Y. Wu, P. Shen, T. Yan, X. Li, Y. Song, Z. Zha, X. Han, Controlled CRISPR-Cas9 Ribonucleoprotein Delivery for Sensitized Photothermal Therapy, Small 17 (33) (2021) e2101155.
[35] C. Chen, W. Zhong, S. Du, Y. Li, Y. Zeng, K. Liu, J. Yang, X. Guan, X. Han, Intelligent nanotherapeutic strategies for the delivery of CRISPR system, Acta Pharm Sin B 13 (6) (2023) 2510–2543, https://doi.org/10.1016/j.apsb.2022.12.013.
[36] S.Y. Liu, Y. Xu, H. Yang, L. Liu, M. Zhao, W. Yin, Y.T. Xu, Y. Huang, C. Tan, Z. Dai, H. Zhang, J.P. Zhang, X.M. Chen, Ultrathin 2D Copper(I) 1,2,4-Triazolate Coordination Polymer Nanosheets for Efficient and Selective Gene Silencing and Photodynamic Therapy, Adv Mater 33 (18) (2021) e2100849.
[37] C. Xing, Q. Lin, Y. Chen, S. Zeng, J. Wang, C. Lu, A smart metal-polyphenol-DNAzyme nanoplatform for gene-chemodynamic synergistic tumor therapy, Acta Biomater 167 (2023) 564–573, https://doi.org/10.1016/j.actbio.2023.05.042.
[38] C. Liu, Y. Chen, J. Zhao, Y. Wang, Y. Shao, Z. Gu, L. Li, Y. Zhao, Self-Assembly of Copper-DNAzyme Nanohybrids for Dual-Catalytic Tumor Therapy, Angew Chem Int Ed Engl 60 (26) (2021) 14324–14328, https://doi.org/10.1002/anie.202101744.